GEOPHYSICS, VOL. 82, NO. 5 (SEPTEMBER-OCTOBER 2017); P. C163–C174, 21 FIGS.
10.1190/GEO2016-0375.1

Elastic full-waveform inversion for VTI media: A synthetic parameterization study

Nishant Kamath[1], Ilya Tsvankin[1], and Esteban Díaz[2]

ABSTRACT

One of the main challenges for full-waveform inversion (FWI) is taking into account both anisotropy and elasticity. Here, we perform elastic FWI for a synthetic 2D VTI (transversely isotropic with a vertical symmetry axis) model based on the geologic section at Valhall field in the North Sea. Multicomponent surface data are generated by a finite-difference code. We apply FWI in the time domain using a multiscale approach with three frequency bands. An approximate inverse Hessian matrix, computed using the L-BFGS-B algorithm, is employed to scale the gradients of the objective function and improve the convergence. In the absence of significant diving-wave energy in the deeper part of the section, the model is updated primarily with reflection data. An oblique displacement source, which excites sufficiently intensive shear waves in the conventional offset range, helps provide more accurate updates in the Shear-wave vertical velocity, especially in the shallow layers. We test three model parameterizations, which exhibit different radiation patterns and, therefore, create different parameter trade-offs. Whereas most examples are for a constant-density model, we also generate a density field using Gardner's relationship and invert for the density along with the velocity parameters. The parameterizations that combine velocities and anisotropy coefficients generally yield superior results to the one that includes only velocities, provided that a reasonably accurate initial model is available.

INTRODUCTION

Full-waveform inversion (FWI), as originally proposed by Tarantola (1984), is designed to estimate an earth model that minimizes the difference between the observed and simulated seismic wavefields. The main advantage of this method is the possibility of achieving high resolution by employing the phase and amplitude information contained in the recorded waveforms.

In the initial stages of FWI, it is common to operate with diving-wave energy to update the long-wavelength (or smoothly varying) component of the velocity model. The multiscale approach of Bunks et al. (1995) is typically used to ensure that the inversion algorithm does not get trapped in a local minimum. Once an accurate background model has been obtained, reflection events can be incorporated to improve the vertical resolution of the model.

When FWI is performed for anisotropic media, it is typically done in the acoustic approximation. Plessix and Cao (2011), Gholami et al. (2013b), and Alkhalifah and Plessix (2014) discuss the sensitivity of the FWI objective function to different parameters of acoustic VTI media, where P-wave propagation is controlled by three Thomsen parameters — the vertical velocity V_{P0} and the anisotropy coefficients ϵ and δ. They apply FWI for various combinations of V_{P0}, the P-wave normal moveout (NMO) ($V_{\mathrm{nmo}} = V_{P0}\sqrt{1+2\delta}$), and horizontal ($V_{\mathrm{hor}} = V_{P0}\sqrt{1+2\epsilon}$) velocities and the anisotropy coefficients ϵ, δ, and $\eta = (\epsilon-\delta)/(1+2\delta)$. Optimal parameterization for FWI depends on acquisition geometry, the data used for the inversion (diving waves or reflection events), and type of model updates (simultaneous or hierarchic). Although the acoustic approximation is computationally efficient, it cannot properly model reflection amplitudes and handle shear- and mode-converted waves.

Lee et al. (2010) perform FWI of synthetic surface data for 2D elastic VTI media but describing the model in terms of the stiffness coefficients leads to ambiguity in their results. Sears et al. (2008) develop a methodology to invert multicomponent ocean-bottom cable (OBC) data from isotropic elastic media for short and intermediate length-scale P- and S-wave velocities. Application of this approach to FWI of field data recorded at Alba Field, UK, is presented by Sears et al. (2010). Elastic FWI is employed by Prieux

Manuscript received by the Editor 15 July 2016; revised manuscript received 28 February 2017; published ahead of production 18 May 2017; published online 16 August 2017.
[1]Colorado School of Mines, Golden, Colorado, USA. E-mail: nkamath@mines.edu; ilya@mines.edu.
[2]Formerly Colorado School of Mines, Golden, Colorado, USA; presently BP, Houston, Texas, USA. E-mail: esteban.diaz@bp.com.

et al. (2013) to invert hydrophone and OBC data from the Valhall field in the North Sea. Although their modeling operator accounts for anisotropy, the inversion algorithm updates only the P- and S-wave vertical velocities. Vigh et al. (2014) carry out elastic isotropic FWI of a data set from the Gulf of Mexico. Their algorithm inverts pressure records along with the vertical and horizontal displacements recorded in the OBC survey.

Kamath and Tsvankin (2013) perform elastic FWI of multicomponent data from a horizontally layered VTI model. They show that it is possible to estimate the parameters V_{P0}, ϵ, δ, and the S-wave vertical velocity V_{S0} even for offset-to-depth ratios close to unity, primarily because the algorithm accurately models reflection coefficients. The gradients of the FWI objective function for elastic arbitrarily anisotropic media are presented by Kamath and Tsvankin (2016). They develop a methodology for FWI in 2D elastic VTI media and apply their algorithm to multicomponent data for models with Gaussian anomalies in the Thomsen parameters. Kamath and Tsvankin (2016) also obtain general expressions for "radiation" (i.e., sensitivity) patterns of model parameters for elastic anisotropic FWI and use this formalism to explain their numerical results. However, optimizing parameterization remains a key issue in FWI, especially for anisotropic media.

Here, we analyze parameter resolution and trade-offs in the inversion of multicomponent surface data generated for a realistic 2D elastic VTI model based on the geologic section at the Valhall field. The paper begins with a review of the inversion methodology based on the algorithm of Kamath and Tsvankin (2016). Then, we describe the model used to generate the wavefield and the processing steps applied to the simulated data. A multiscale approach is used to perform FWI in three frequency bands. We discuss the inversion results obtained for different model parameterizations and explain them in terms of the radiation (sensitivity) patterns.

METHODOLOGY

Inversion methodology

We carry out FWI in the time domain by minimizing the following objective function:

$$\mathcal{F} = \frac{1}{2}\sum_{r=1}^{N} \|\mathbf{u}(\mathbf{x}_r, t) - \mathbf{d}(\mathbf{x}_r, t)\|^2, \tag{1}$$

where N is the number of receivers, $\mathbf{u}(\mathbf{x}_r, t)$ is the displacement computed for a trial model at receiver location $\mathbf{x}_r$ and time t, and $\mathbf{d}(\mathbf{x}_r, t)$ is the recorded displacement. Summation over shots is implied. The gradient of $\mathcal{F}$ with respect to the stiffness coefficients c_{ijkl} is obtained using the adjoint-state method (Kamath and Tsvankin, 2016):

$$\frac{\partial \mathcal{F}}{\partial c_{ijkl}} = -\int_0^T \frac{\partial u_i}{\partial x_j}\frac{\partial \psi_k}{\partial x_l}\, dt, \tag{2}$$

where $\mathbf{u}$ and $\boldsymbol{\psi}$ are the forward and adjoint displacement fields, respectively. The gradient for all model parameters m_n except for density (the derivative $\partial\mathcal{F}/\partial\rho$ is given by equation A-22) can be found as

$$\frac{\partial \mathcal{F}}{\partial m_n} = \sum_{ijkl} \frac{\partial \mathcal{F}}{\partial c_{ijkl}}\frac{\partial c_{ijkl}}{\partial m_n}. \tag{3}$$

Signatures of P- and SV-waves in VTI media are governed by four independent parameters. Here, we define the model using three different parameter sets. Parameterization I (Kamath and Tsvankin, 2013) includes the velocities V_{P0}, V_{S0}, V_{nmo}, and V_{hor}; parameterization II consists of the squared velocities V_{nmo}^2 and V_{S0}^2, $(1+2\eta)$, and $(1+2\delta)$; parameterization III is a combination of the squared velocities V_{hor}^2 and V_{S0}^2, $(1+2\eta)$, and $(1+2\epsilon)$. The last two parameter sets (without V_{S0}^2) were suggested and analyzed for acoustic VTI media by Alkhalifah and Plessix (2014). The velocities in parameterizations II and III are normalized by their respective initial values, which makes the corresponding parameters dimensionless and reduces them to same order of magnitude as the anisotropy coefficients. Including density as a model parameter makes the objective function highly nonlinear (Kamath and Tsvankin, 2013), so here, density is fixed at the actual value. The gradients of the objective function (equation 1) for each parameterization are given in Appendix A.

A 2D elastic finite-difference modeling code from the Madagascar package is used to generate the data. To obtain the model update at each iteration, the gradient is scaled by a factor that can be chosen in different ways. In the widely used steepest-descent method, the scaling factor is set equal to the step length, which does not account for the energy loss due to geometric spreading. In the absence of a Hessian term (or its approximation), the gradient is too large near the sources and receivers, which complicates velocity estimation. Therefore, the gradients at the source and receiver locations have to be masked to ensure meaningful model updates. In addition, the steepest-descent technique could produce slow convergence if the objective function has a long and narrow "valley."

The problems associated with the steepest-descent algorithm can be circumvented by applying the Gauss-Newton method and computing the model update $\Delta\mathbf{m}$ from

$$\Delta\mathbf{m} = \alpha[\mathcal{H}]^{-1}\mathbf{G}, \tag{4}$$

where α is the step length, $\mathcal{H}$ is the Hessian operator and $\mathbf{G}$ is the gradient of the objective function, whose derivatives are defined in equation 3. Computation of the Hessian, however, is extremely expensive. The Broyden-Fletcher-Goldfarb-Shanno (BFGS) algorithm or its low-memory equivalent (L-BFGS) is often used to obtain an approximate Hessian. Here, we use the L-BFGS-B (bounded) package of Byrd et al. (1995) to compute the operator $\mathcal{H}$ and update the model from equation 4.

Synthetic model and data processing

The synthetic model used here is based on the VTI parameters estimated for the Valhall field in the North Sea (Munns, 1985). The V_{P0} field (Figure 1a) includes low-velocity gas layers above the reservoir, which is located at a depth of 2.5 km. The original model is sampled every 3.125 m in the horizontal and vertical directions. However, to reduce computational time in the finite-difference modeling, the grid spacing here is increased to 20 m. Although the original Valhall model has a water column on top, we make the entire section elastic and clip the S-wave velocity V_{S0} so that its minimum value near the surface is equal to 700 m/s.

Multicomponent synthetic data are generated by a horizontal array of displacement sources (their orientation is specified below) placed with an 80 m increment at a depth of 20 m. The receivers are located at every grid point at the same depth (20 m). The source signal is a Ricker wavelet with a peak frequency of 3.5 Hz. We use absorbing boundary conditions at the surface and, hence, do not generate surface-related multiples or ground roll.

To better understand the wavefield, we shoot a fan of diving (refracted) rays from two source locations using a VTI ray-tracing program (`sfrays2a`) in Madagascar (Figure 2). Most of the P-wave diving-wave energy is limited to depths down to 1.5 km, although shots at the edges of the survey produce diving waves that penetrate down to approximately 2.5 km. In addition to diving waves, we record reflections from the shallow gas layers, which should allow us to achieve relatively high spatial resolution for the top 1.5 km of the section. The laterally extended version of this model in Gholami et al. (2013a) makes it possible to acquire diving waves from the layer immediately above the reservoir, where our model produces only reflections.

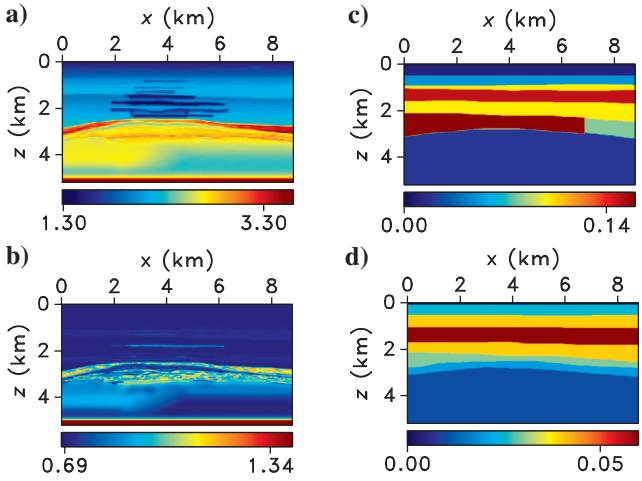

Figure 1. Parameters (a) V_{P0}, (b) V_{S0}, (c) ϵ, and (d) δ of a synthetic model based on sections from the Valhall field. The velocities here and in the subsequent plots have units of km/s.

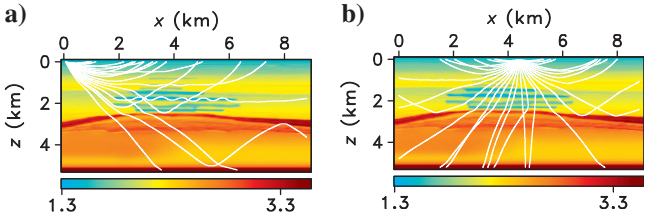

Figure 2. Fans of rays from sources at (a) $x = 0$ km and (b) $x = 4.4$ km superimposed on the actual V_{P0} field.

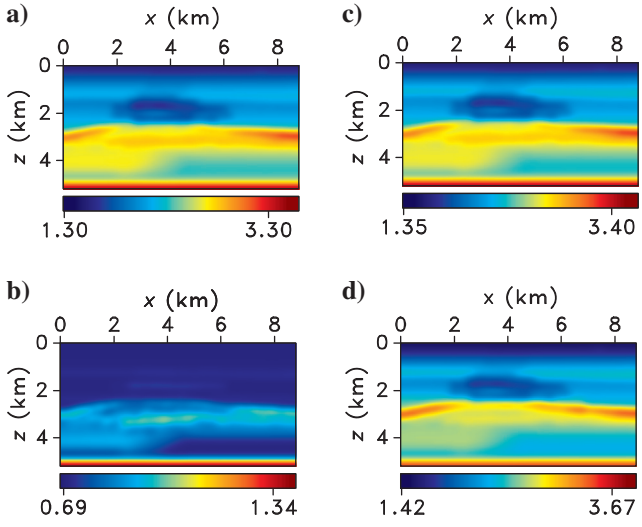

Figure 3. Initial model for the velocities (a) V_{P0}, (b) V_{S0}, (c) V_{nmo}, and (d) V_{hor}.

The actual fields of the velocities V_{P0}, V_{S0}, V_{nmo}, and V_{hor} are smoothed (using a triangular filter with a radius of 10 samples, applied three times) to generate the initial model for FWI using parameterization I (Figure 3). The initial models for parameterizations II and III are computed from the initial velocities in Figure 3. The vertical variation of the actual coefficient δ is much smoother than that of ϵ, which has large jumps at depths of 1.7 and 2.2 km. Hence, the difference between the initial and actual ϵ- and η-fields reaches maximum values of approximately 0.08 (Figures 4e and 4g, respectively), whereas the initial δ is more accurate. However, the deviations of the initial ϵ, η, and δ-fields from the actual models are relatively small.

The L-BFGS-B implementation requires putting bounds on the model parameters, so each velocity is bounded by its minimum and maximum values for the actual model. As mentioned above, FWI is applied with the actual density field. We carry out the inversion using

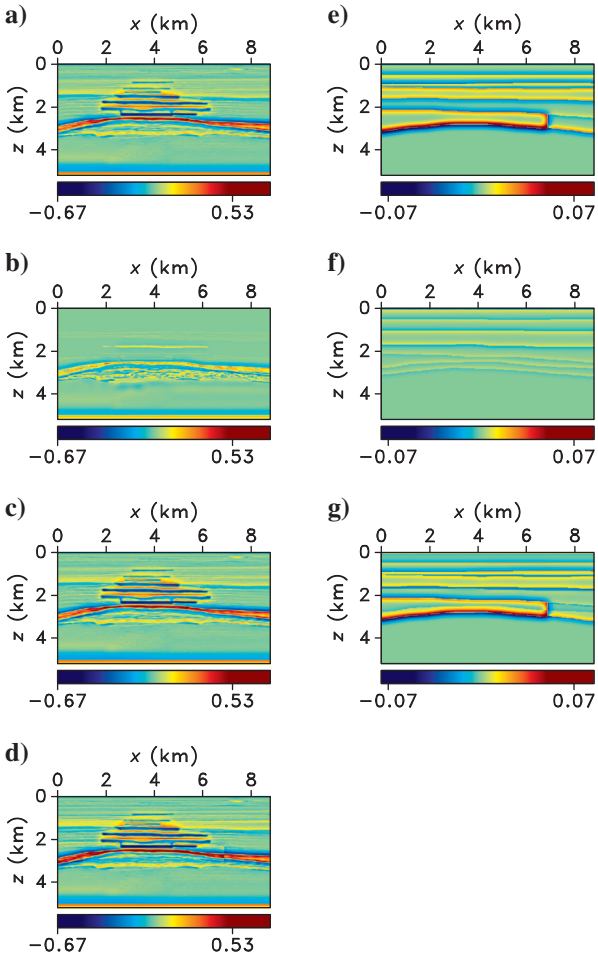

Figure 4. Difference between the actual and initial models: (a) V_{P0}, (b) V_{S0}, (c) V_{nmo}, (d) V_{hor}, (e) ϵ, (f) δ, and (g) η.

a multiscale approach with the following frequency bands: 0–3, 0–5, and 0–7 Hz. The inversion results for each frequency band provide the initial models for the next (higher frequency) band. For this range of frequencies, FWI is unlikely to resolve some high-resolution features of the actual velocity fields (Figure 4a–4d). Although including higher frequencies should improve resolution, we restrict the frequency range to reduce the computational cost.

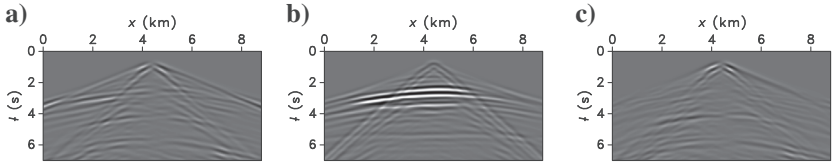

Figure 5. (a) Horizontal and (b) vertical displacement components of the difference between the observed data and those computed for the initial model in the 0–5 Hz frequency range. The (c) horizontal and (d) vertical components of the difference between the observed data and those computed for the inverted model. The data are generated by an array of vertical displacement sources. The displacement components are plotted on the same scale.

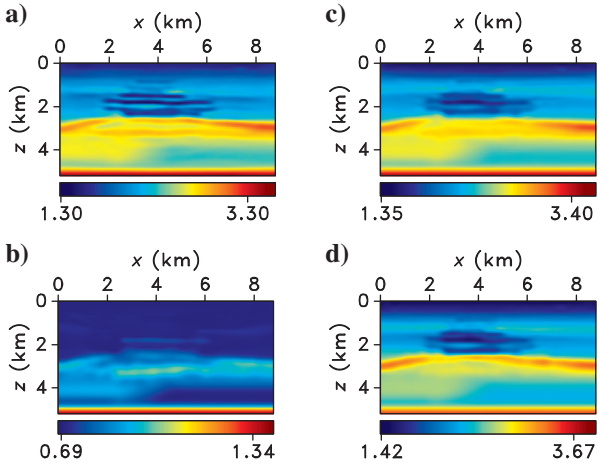

Figure 6. Inverted velocities (a) V_{P0}, (b) V_{S0}, (c) V_{nmo}, and (d) V_{hor} for parameterization I. The data were generated by an array of vertical displacement sources.

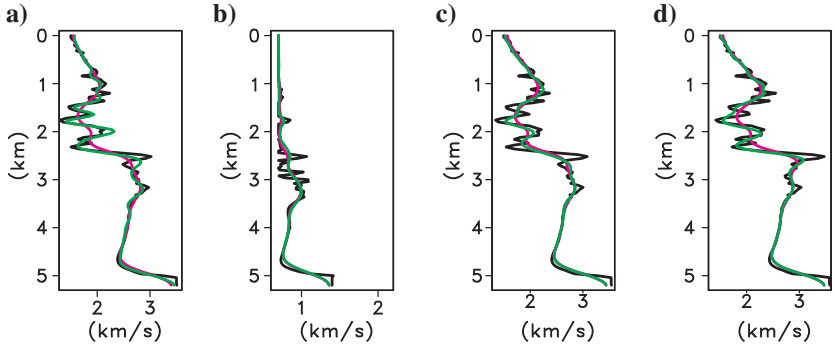

Figure 7. Actual (black), initial (magenta), and inverted (green) velocities for parameterization I: (a) V_{P0}, (b) V_{S0}, (c) V_{nmo}, and (d) V_{hor}. The data were generated by an array of vertical displacement sources. The profiles here and in the subsequent plots are displayed at location $x = 3.5$ km.

NUMERICAL TESTS

Parameterization I (V_{P0}, V_{S0}, V_{nmo}, V_{hor})

The first test is performed for parameterization I with the wavefield generated by vertical displacement sources. Figure 5 illustrates the improvement in data fit between the initial and inverted models for the 0–5 Hz frequency band.

Figures 6a and 7a indicate that the shallow-gas layers are generally well delineated by low-velocity anomalies in the updated V_{P0}-field. However, lack of frequencies above 7 Hz in the data limits the spatial resolution of the inverted V_{P0} and results in errors at depths of about 1.2, 2.2, and 2.5 km (Figure 7a). The relatively low amplitude of shear waves produced by a vertical source does not allow the algorithm to properly update V_{S0} (Figure 7b). Although the inverted velocity V_{nmo} matches the trend of the actual curve more closely than the initial model (Figure 7c), the spatial resolution in V_{nmo} is lower than that for V_{P0} (compare Figures 6a and 6c), with noticeable deviations at depths of 1.2, 1.5, 2.2, and 2.5 km. The low-frequency trend of the V_{hor} field, especially at depths of 1.5, 1.8, 2, and 2.2 km, closely resembles the actual curve (Figure 7d).

The P-wave radiation patterns (see Appendix B) of the model parameters (Figure 8a) can help explain the obtained results (Kamath and Tsvankin, 2016). A V_{P0}-anomaly on a horizontal reflector scatters P-wave energy mostly near the vertical symmetry axis, which results in a relatively high vertical resolution of the updated V_{P0} field (Wu and Toksöz, 1987). In the case of an anomaly in V_{hor}, most of the energy is scattered near the horizontal isotropy plane, which explains why the updates in the horizontal velocity are mostly confined to the middle part of the model probed by large-angle reflections. Diving waves and large-angle reflections are largely responsible for long-wavelength updates, whereas conventional-offset reflections improve the spatial resolution of the model (Wu and Toksöz, 1987). The resolution provided by diving waves in FWI (typically on the order of a wavelength) is, however, higher than that obtained from traveltime tomography, in which the resolution is limited by the first Fresnel zone (Williamson, 1991). Overall, the velocity V_{hor} is estimated with a higher accuracy compared with V_{nmo} but has a lower spatial resolution than V_{P0} and V_{nmo}.

The maximum energy of P-waves scattered by a V_{nmo}-anomaly (Figure 8) is only about 25% of that for V_{P0} and is focused at opening angles near 90° (which correspond to incidence angles of about 45°). Therefore, the algorithm cannot update V_{nmo} at depths below 2.4 km. Scattering by an anomaly in V_{S0} has a pattern similar to that in V_{nmo}, which causes a trade-off between the two velocities. The radiation patterns in Figures 8, 9, and 10 assume a background V_P/V_S-ratio of two, for which the energy scattered by an anomaly in V_{S0} is higher than that for V_{nmo}. However, for the model used in this paper, the V_{P0}/V_{S0}-ratio reaches values of up to three between the depths of 0.5 and 2.5 km. The increase in the V_{P0}/V_{S0}-ratio reduces the magnitude of the V_{S0}-radiation pattern, which leads to a more significant trade-

off between V_{S0} and V_{nmo} and inaccurate updates in V_{S0} from the P-wavefield. Based on the S-wave radiation patterns (Figure 8b), we expect significant updates in the V_{S0}-field from near- and far-offset shear-wave data. However, a vertical displacement source does not generate sufficiently intensive shear waves in the recorded offset range, which suppresses updates in V_{S0}.

One of the advantages of parameterization I is the insignificant trade-off between the velocities V_{P0} and V_{hor}. The P-wave radiation patterns (Figure 8a) suggest that near-offset data are largely responsible for updating the V_{P0}-field, whereas long-offset data and diving waves should help constrain V_{hor}. However, the inversion results for V_{hor} are satisfactory only in the shallow region (above 2 km), for which the offset-to-depth ratio is sufficiently large. Hence, if long-offset data (with the offset-to-depth ratio of two or more) are available, diving waves can be inverted for an accurate low-wavenumber V_{hor}-field. In the deeper layers, the estimates of V_{hor} and the parameter ϵ (obtained from the relation $V_{\text{hor}} = V_{P0}\sqrt{1+2\epsilon}$) are unsatisfactory. Likewise, the updates in V_{nmo} have a lower magnitude and vertical resolution compared with those in V_{P0}, thereby resulting in the distorted δ field computed from the equation $V_{\text{nmo}} = V_{P0}\sqrt{1+2\delta}$.

Overall, parameterization I helps resolve the P-wave vertical velocity V_{P0}, but the other Thomsen parameters for our synthetic survey are not well-constrained. There is no trade-off between V_{P0} and the other velocities for relatively small opening angles, which ensures accurate V_{P0} updates. Hence, if only conventional-offset data (with the maximum offset-to-depth ratio close to unity) are available, it is advantageous to invert for V_{P0} using parameterization I.

Next, we perform FWI for data generated with an oblique displacement source, whose vertical and horizontal components are equal. If the subsurface layer is isotropic, the maximum of the source radiation pattern is in the direction of the source for P-waves and orthogonal to it for SV-waves (Figure 11). Therefore, the oblique source generates more intensive shear waves in the recorded offset range, which results in larger, more accurate updates for the V_{S0}-field, especially in the 1–1.5 km depth range (Figure 12b). Indeed, whereas the P-wave velocity V_{P0} is sensitive to energy propagating at small opening angles, V_{S0} is largely influenced by P- and SV-wave energy at intermediate angles near 45°.

The SV-wave radiation patterns for anomalies in the velocities V_{nmo} and V_{hor} are identical; both have trade-offs with V_{S0} for intermediate opening angles (Figure 8b). This causes insufficiently large updates in V_{nmo} and V_{hor} (compare Figures 7 and 12) at depths of 1.8 km and 2.2 km, and incorrect updates in V_{S0} at 2.2 km. However, for depths down to 1.8 km, the 45°-rotation of the source produces an improvement in all four inverted velocities. Overall, intensive S-waves bring in more information and help resolve the V_{S0}-

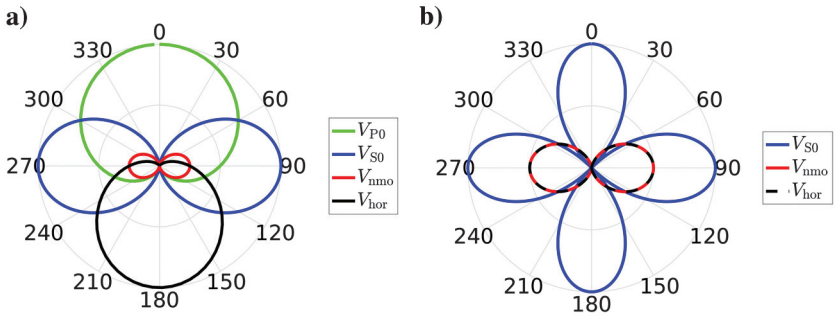

Figure 8. (a) P- and (b) SV-wave radiation patterns obtained with parameterization I for reflections from a horizontal interface. The patterns here and in the subsequent plots are computed as functions of the opening angles at a point on a reflector with the background $V_P/V_S = 2$.

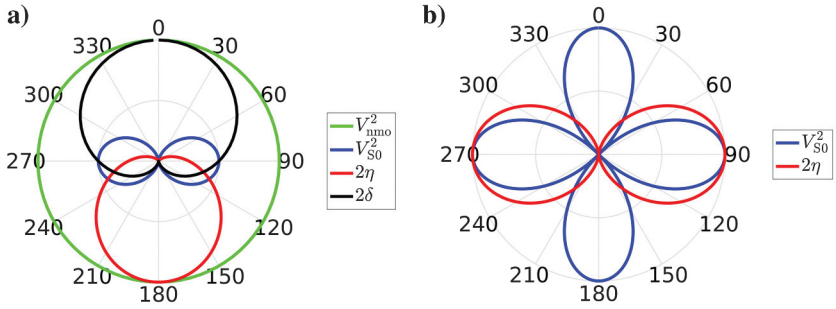

Figure 9. (a) P- and (b) SV-wave radiation patterns obtained with parameterization II for reflections from a horizontal interface.

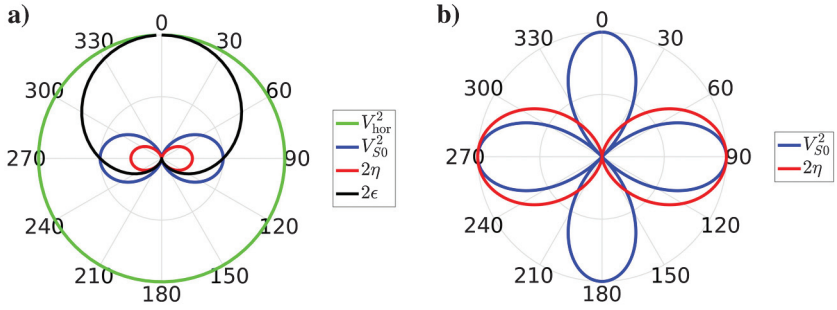

Figure 10. (a) P- and (b) SV-wave radiation patterns obtained with parameterization III for reflections from a horizontal interface.

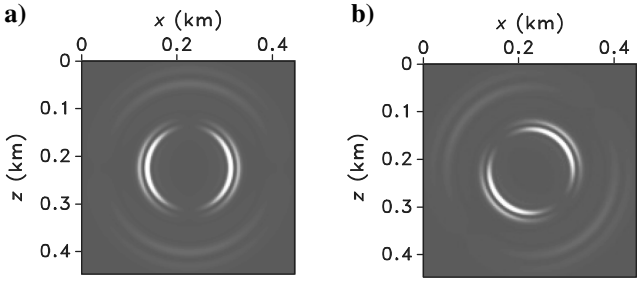

Figure 11. Magnitude of displacement generated by (a) a vertical and (b) an oblique (tilted by 45°) displacement source located at the center of the plot in a homogeneous elastic isotropic medium.

field, although they create additional trade-offs for parameterization I. Still, to exploit the shear-wave information, the oblique source is used in all tests for the other two parameterizations.

For the low frequencies used in these tests, comparable results were obtained with a less accurate initial model generated by stronger smoothing (the same triangular filter as before, but applied ten times) of the actual parameter fields.

To reduce computational cost, we do not compute synthetic data for times exceeding 7 s. Increasing the trace length to about 12 s allows us to capture shear-wave arrivals at larger offsets, which results in better updates in V_{S0}. The trade-off between V_{S0} and other parameters, however, causes deterioration in the estimates of V_{P0}, V_{nmo}, and V_{hor}. More accurate results for the longer recordings can be obtained either by inverting for V_{S0} separately after the other three parameters have been updated or by downscaling shear arrivals at long offsets (Duan et al., 2017).

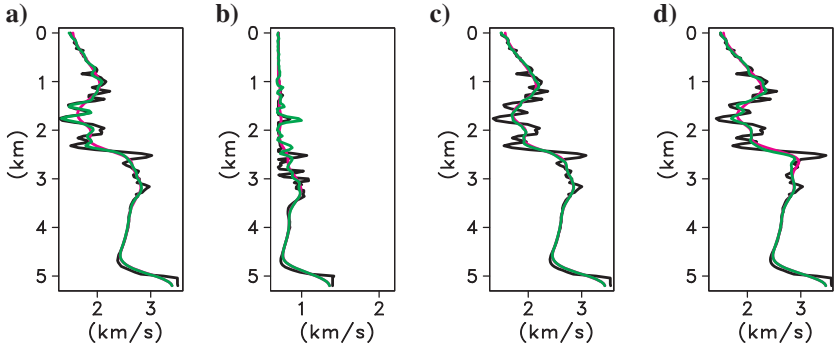

Figure 12. Actual (black), initial (magenta), and inverted (green) velocities for parameterization I: (a) V_{P0}, (b) V_{S0}, (c) V_{nmo}, and (d) V_{hor}. The data here and in the subsequent plots are generated by an array of oblique displacement sources.

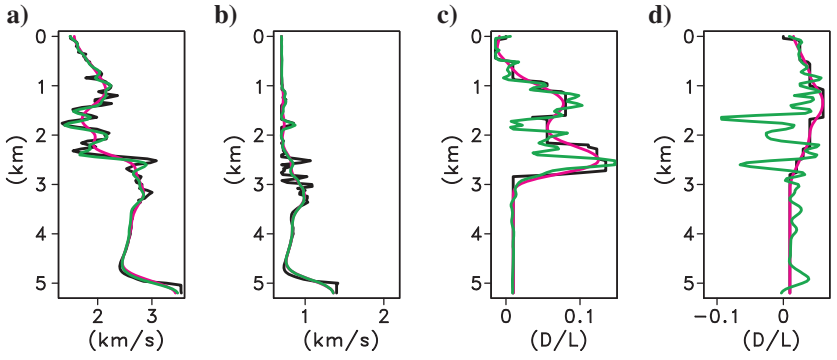

Figure 13. Actual (black), initial (magenta), and inverted (green) parameters for parameterization II: (a) V_{nmo}, (b) V_{S0}, (c) η, and (d) δ.

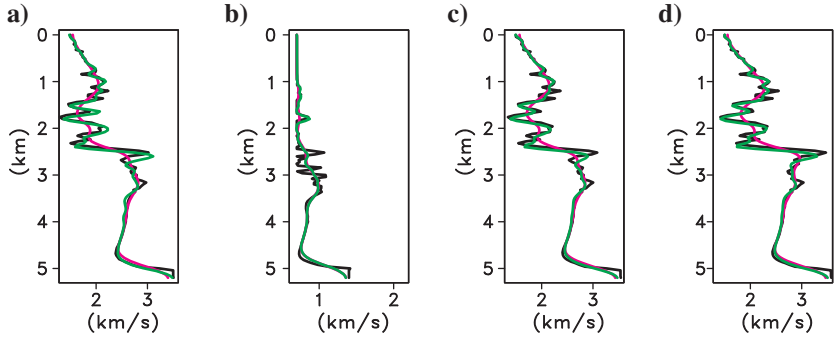

Figure 14. Actual (black), initial (magenta), and inverted (green) velocities for parameterization II: (a) V_{P0}, (b) V_{S0}, (c) V_{nmo}, and (d) V_{hor}. The velocities V_{P0} and V_{hor} are computed from the estimated V_{nmo}, δ, and η.

Parameterization II (V^2_{nmo}, V^2_{S0}, $1+2\eta$, $1+2\delta$)

Next, we perform the inversion using parameterization II, which includes V^2_{nmo}, V^2_{S0}, $(1+2\eta)$, and $(1+2\delta)$; the velocities are normalized by their respective initial values. The P-wave radiation pattern of an anomaly in V_{nmo} is "isotropic" (Figure 9a), with energy evenly scattered over the full range of angles. Plessix and Cao (2011) employ the combination (V_{nmo}, η, and δ) for FWI in acoustic VTI media and demonstrate that V_{nmo} is more tightly constrained than η and δ, whose estimation is hampered by large null-spaces. The radiation patterns exhibit trade-offs between V_{nmo} and δ for small opening angles and between V_{nmo} and η for large angles (Figure 9a).

The P- and SV-wave radiation patterns for V_{S0} are similar to those for parameterization I. The SV-wave radiation patterns (Figure 9b) indicate trade-offs between V_{S0} and η for intermediate opening angles (incidence angles of around 45°). The updates in the V_{S0}-field are accurate down to a depth of 2 km (Figure 13b), which indicates that the objective function is more sensitive to the velocity V_{S0} than to the coefficient η. More intensive P- and SV-waves at incident angles near 45° generated by the oblique source produce better updates in the parameters V_{hor}, V_{S0}, and η compared to tests with the vertical source. Indeed, the radiation patterns indicate that the objective function is more sensitive to those three parameters at intermediate opening angles.

The decrease in the objective function for this parameterization is, in general, larger for all three frequency bands compared to that for parameterization I. A purely isotropic P-wave radiation pattern for V_{nmo} combined with a higher sensitivity to this velocity makes parameterization II most suitable for estimating V_{nmo} from data recorded for a wide offset range. Indeed, employing parameterization II results in a marked improvement (compared to parameterization I) in the V_{nmo} field. At depths of 1.2 km, 2.2 km, and 2.5 km (Figure 13a), the inverted V_{nmo} matches the actual values better than for parameterization I. Because the initial η- and δ-fields are relatively close to the actual models, the updates in both anisotropy coefficients are insignificant (Figures 13c and 13d). An accurate inverted V_{nmo}-field combined with just slightly distorted anisotropy coefficients yields good estimates of the velocities V_{P0} and V_{hor}. The V_{P0}-profile (Figure 14a) matches the true values at depths of 1.2 km, 2.2 km, and 2.5 km even more closely than for parameterization I (Figure 7a). Figure 14d

illustrates an improvement in the spatial resolution of the inverted V_{hor}-field as well (compared with Figure 7d at depths of 1.2 km, 1.7 km, 2.2 km, and 2.5 km).

Migration velocity analysis in VTI media can recover smooth fields of V_{nmo} and η (or V_{hor}) (e.g., Tsvankin, 2012), but errors in the parameter δ are typically higher. Hence, next we add a constant value of 0.1 to the initial δ-field used before. Such an overestimated δ yields understated initial velocities V_{P0} which move the imaged reflectors up toward the surface (Plessix and Cao, 2011). With parameterization II, V_{P0} is not updated directly; also, the updates in the anisotropy coefficients η and δ remain relatively small (Figures 15c and 15d, respectively). Consequently, the estimated V_{nmo}- and V_{hor}-fields are shifted vertically with respect to the actual model. Therefore, parameterization II should be useful in cases when not only a wide range of offsets is recorded, but also prior estimates of the η- and δ-fields are sufficiently accurate.

Parameterization III (V_{hor}^2, V_{S0}^2, $1+2\eta$, $1+2\epsilon$)

Finally, the inversion is carried out for parameterization III [V_{hor}^2, V_{S0}^2, $(1+2\eta)$, and $(1+2\epsilon)$], with the velocities normalized by their initial values. The P- and SV-wave radiation patterns for an anomaly in V_{S0} are similar for all three parameterizations, and the SV-wave pattern for η coincides with that for parameterization II. For parameterization III, the velocity V_{hor} has a purely isotropic P-wave radiation pattern (Figure 10a), which was the case for V_{nmo} in parameterization II. Trade-offs exist between V_{hor} and ϵ for small opening angles, and between V_{hor} and η for intermediate opening angles (which correspond to incidence angles close to 45°). Because V_{hor} has no trade-offs with any other parameter for large opening angles, diving waves can be employed to accurately update the long-wavelength V_{hor}-field (Alkhalifah, 2015). As was the case for parameterization II, tilting the source by 45° from the vertical improves inversion results. In addition, the objective function decreases faster than for parameterization I.

In agreement with the results of Alkhalifah (2015) and Oh and Alkhalifah (2016), for this parameterization, V_{hor} is the best constrained parameter (Figure 16a). The updates in the η- and ϵ-fields, which are relatively close to the actual values to begin with, are insignificant (Figures 16c and 16d, respectively). The inverted V_{hor}-field is similar to that obtained with parameterization II (compare Figures 17d and 14d). In addition, because the inverted values of η and ϵ are fairly accurate, the V_{P0}- and V_{nmo}-fields estimated from V_{hor} and the anisotropy coefficients are also well-resolved and resemble those for parameterization II. A distorted initial ϵ-field computed from the erroneous δ-model used before yields the inverted

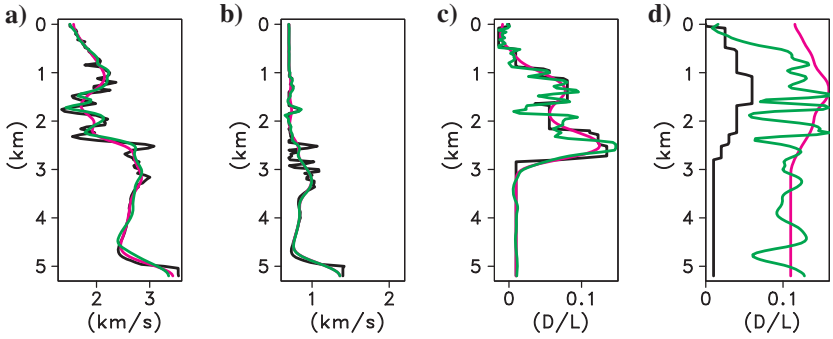

Figure 15. Actual (black), initial (magenta), and inverted (green) parameters for parameterization II: (a) V_{nmo}, (b) V_{S0}, (c) η, and (d) δ. Inversion is performed for the distorted initial δ obtained by adding 0.1 to the initial δ field used in previous examples.

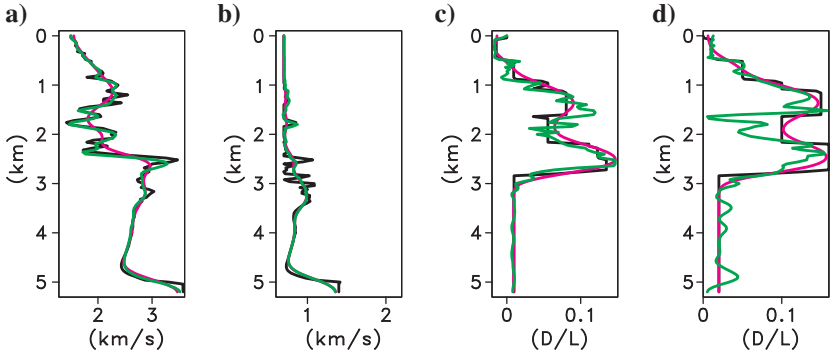

Figure 16. Actual (black), initial (magenta), and inverted (green) parameters for parameterization III: (a) V_{hor}, (b) V_{S0}, (c) η, and (d) ϵ.

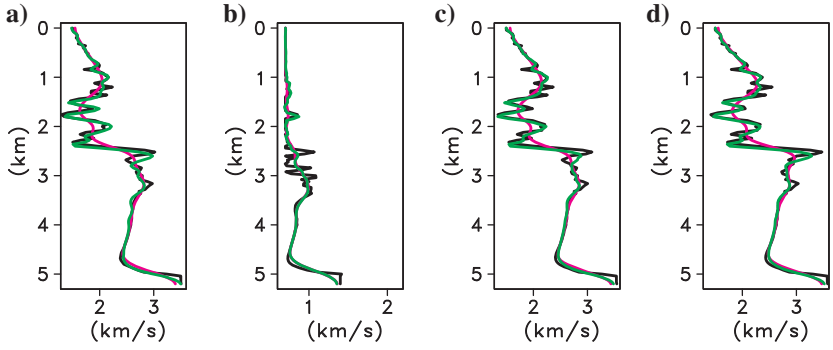

Figure 17. Actual (black), initial (magenta), and inverted (green) velocities for parameterization III: (a) V_{P0}, (b) V_{S0}, (c) V_{nmo}, and (d) V_{hor}.

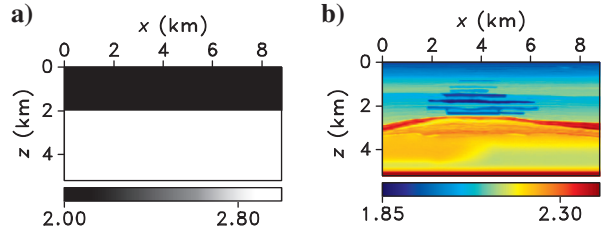

Figure 18. (a) Two-layer density model and (b) the density field calculated from Gardner's relationship. The units here and in subsequent plots are g/cm^3.

velocities V_{hor} and V_{nmo} with vertical shifts, as was the case for parameterization II.

The main advantage of this parameter combination over parameterization II is that diving waves can be inverted for an accurate low-wavenumber V_{hor}-field. High-resolution estimates of V_{hor} can be obtained from conventional offsets if the coefficient ϵ is well-constrained a priori.

INFLUENCE OF DENSITY

When FWI is performed for elastic media, it is important to understand the influence of density on the inverted parameters. In the previous tests, the density was constant and fixed at the correct value. Here, we conduct experiments with data generated for two density models (the other parameters are unchanged): one includes two homogeneous layers (Figure 18a), and the other is created using Gardner's (Gardner et al., 1974) relationship between the density ρ and P-wave velocity ($\rho = 0.31V_{P0}^{0.25}$; Figure 18b). The P- and SV-wave radiation patterns for density (Figure 19) are the same for all three parameterizations. For parameterizations II and III, the trade-offs between density and the velocities V_{nmo} and V_{hor} (respectively) are less pronounced than that between density and V_{P0} in parameterization I. Hence, we use parameterization III for the tests below; parameterization II is expected to give similar results.

Although the initial velocity parameters are the same (Figure 3), the understated density below 2 km leads to an increase in the inverted velocities V_{hor} and V_{S0}, which causes stretching of the velocity fields in the vertical direction (Figure 20a). The distortion in density also produces additional errors in the ϵ- and η-fields. The influence of density may be less significant if the objective function is based on matching just the phase spectra of the observed and modeled data.

The initial density model for the second test (Figure 18b) is obtained by applying the same smoothing operator as the one for the other parameters. To invert for density, we use parameterization III and the corresponding derivative of the objective function with respect to density given by equation A-22. The P-wave radiation pattern for density (Figure 19) indicates a trade-off with the coefficient ϵ resulting in a strong imprint of inaccurate density on the ϵ-field (Figure 21d). In addition, the trade-off between the density and horizontal velocity for small opening angles suppresses updates in V_{hor}, which leads to an upward shift in the velocity models. Because of the inherent trade-offs between velocity and density, improved results could be obtained by reparameterizing the model in terms of velocity and P-wave impedance (Operto et al., 2013).

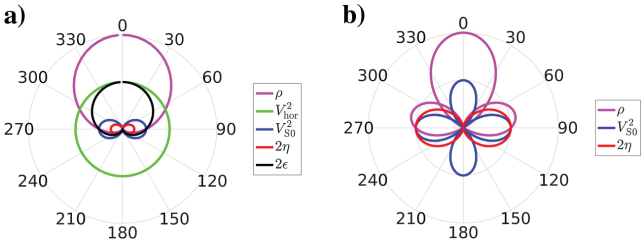

Figure 19. (a) P- and (b) SV-wave radiation patterns including that for the density ρ obtained with parameterization III for reflections from a horizontal interface. The patterns for the velocity parameters have the same shape as those in Figure 10.

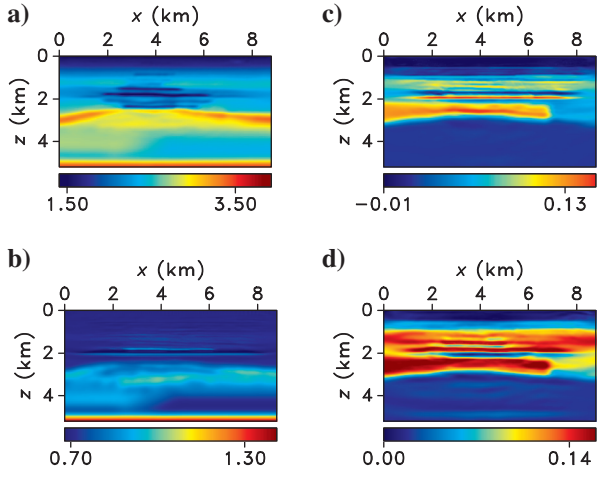

Figure 20. Inverted velocities (a) V_{hor} and (b) V_{S0} and the anisotropy coefficients (c) η and (d) ϵ for parameterization III. The input data were generated for the density field in Figure 18a and inverted using the constant $\rho = 2$ gm/cm^3 for the entire model.

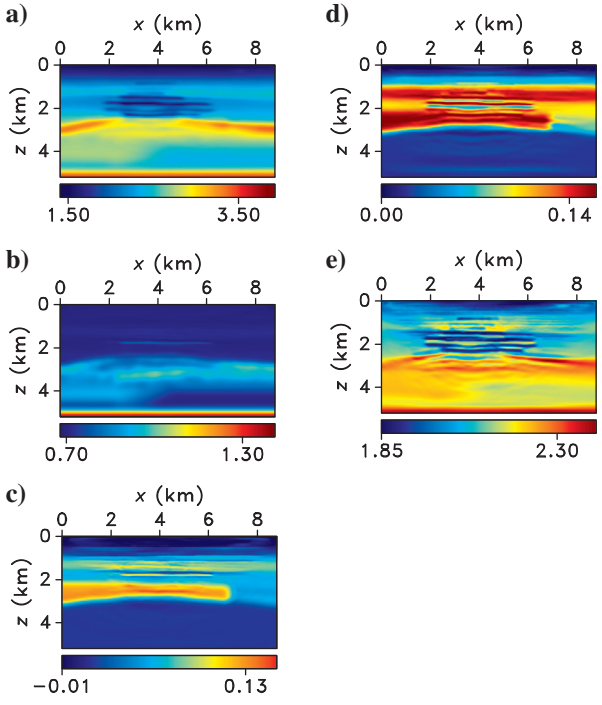

Figure 21. Inverted velocities (a) V_{hor} and (b) V_{S0}, the anisotropy coefficients (c) η, and (d) ϵ, and (e) density for parameterization III. The input data were generated for the model from Figure 3 and the density field from Figure 18b.

CONCLUSION

We presented the results of elastic FWI for a 2D synthetic VTI model similar to the geologic section at the Valhall field in the North Sea. The inversion is carried out in the time domain with the gradients scaled by the inverse of an approximate Hessian matrix estimated using the L-BFGS-B algorithm. Diving waves mostly illuminate the top 1.5 km of the model, so the updates in the deeper regions are provided largely by reflected energy.

The performance of FWI is tested for three different model parameterizations using vertical and oblique displacement sources. The first parameterization includes the P-wave vertical (V_{P0}), NMO (V_{nmo}) and horizontal (V_{hor}) velocities and the shear-wave vertical velocity (V_{S0}). The P-wave radiation patterns of V_{P0} and V_{hor} do not significantly overlap, and the objective function is most sensitive to these two velocities. A high-resolution V_{P0}-field can be obtained even with conventional-offset data if the initial model does not produce cycle-skipping. To build an accurate low-wavenumber model of V_{hor}, it is necessary to use diving waves. For this parameterization, a vertical displacement source, which generates strong P-wave energy at small incidence angles, yields superior inversion results compared to an oblique source.

The objective function for the second parameterization, which consists of V_{nmo}^2, V_{S0}^2, $(1+2\eta)$, and $(1+2\delta)$, is more sensitive to the velocity V_{nmo} than to the other parameters. Because of the trade-off between V_{nmo} and the anisotropy coefficient η at large offsets, the long-wavelength model of V_{nmo} cannot be built without good a priori knowledge of η. The possibility of obtaining a high-resolution V_{nmo}-field from data in the conventional offset range depends on the quality of the initial δ-field. If sufficiently accurate initial estimates of the anisotropy coefficients are available, V_{nmo} is better constrained with parameterization II than parameterization I.

A low-wavenumber model of the horizontal velocity for parameterization III [V_{hor}^2, V_{S0}^2, $(1+2\eta)$, and $(1+2\epsilon)$] can be accurately estimated by inverting long-offset data because there are no trade-offs between V_{hor} and other parameters at large opening angles. Conventional-offset data can yield a high-resolution model of V_{hor} provided the ϵ-field is known with sufficient accuracy.

The inversion results for parameterizations II and III are similar because, in both cases, the objective function is more sensitive to the velocities (V_{nmo} and V_{hor}, respectively) than to the anisotropy coefficients. If the initial long-wavelength anisotropy-parameter fields are accurate (which is the case here), they can be used in conjunction with the inverted V_{nmo} and V_{hor} to obtain V_{P0}. For both parameterizations (II and III), an oblique displacement source provides better updates in V_{S0} than a vertical source.

We also analyzed the errors in the inverted parameters caused by distortions in the density model. Including density in the inversion causes trade-offs with other parameters and deterioration in the inversion results, such as vertical shifts in the velocity fields.

The results for this synthetic model provide important insights into the performance of elastic FWI for VTI media and should help in choosing the most suitable parameterization for different acquisition and inversion scenarios.

ACKNOWLEDGMENTS

We are grateful to the members of the A(nisotropy) and i(maging) teams at CWP and to Chunlei Chu and Phuong Vu (BP) for fruitful discussions. The reviews of associate editor Stéphane Operto and three referees helped improve the paper. The fields of V_{P0}, V_{S0}, ϵ, and δ were provided by Romain Brossier (Université Joseph Fourier, Grenoble) and Olav Barkved (Petoro, Norway). This work was supported by the Consortium Project on Seismic Inverse Methods for Complex Structures at CWP and competitive research funding from King Abdullah University of Science and Technology (KAUST). The reproducible numerical examples are generated with the Madagascar open-source software package freely available from http://www.ahay.org.

APPENDIX A

GRADIENTS FOR DIFFERENT PARAMETERIZATIONS

The gradient of the objective function with respect to the stiffness coefficients c_{ijkl} is given in equation 2. Expressing the stiffnesses in terms of chosen model parameters m_n makes it possible to obtain the gradients with respect to m_n from equation 3. Kamath and Tsvankin (2016) derive the following gradients for VTI media with respect to the velocities V_{P0}, V_{S0}, V_{nmo}, and V_{hor}:

$$\frac{\partial \mathcal{F}}{\partial V_{P0}} = -2\rho V_{P0} \int_0^T \left[\frac{\partial \psi_3}{\partial x_3}\frac{\partial u_3}{\partial x_3} + \frac{f}{2}\left(\frac{\partial \psi_1}{\partial x_1}\frac{\partial u_3}{\partial x_3} + \frac{\partial \psi_3}{\partial x_3}\frac{\partial u_1}{\partial x_1} \right) \right] dt, \tag{A-1}$$

$$\frac{\partial \mathcal{F}}{\partial V_{S0}} = 2\rho V_{S0} \int_0^T \left\{ \left[1 + \frac{f}{2} + \frac{1}{2f} \right] \left(\frac{\partial \psi_1}{\partial x_1}\frac{\partial u_3}{\partial x_3} + \frac{\partial \psi_3}{\partial x_3}\frac{\partial u_1}{\partial x_1} \right) - \left(\frac{\partial \psi_1}{\partial x_3} + \frac{\partial \psi_3}{\partial x_1} \right) \left(\frac{\partial u_1}{\partial x_3} + \frac{\partial u_3}{\partial x_1} \right) \right\} dt, \tag{A-2}$$

$$\frac{\partial \mathcal{F}}{\partial V_{\text{nmo}}} = -\rho V_{\text{nmo}} \int_0^T \frac{1}{f} \left(\frac{\partial \psi_1}{\partial x_1}\frac{\partial u_3}{\partial x_3} + \frac{\partial \psi_3}{\partial x_3}\frac{\partial u_1}{\partial x_1} \right) dt, \tag{A-3}$$

$$\frac{\partial \mathcal{F}}{\partial V_{\text{hor}}} = -2\rho V_{\text{hor}} \int_0^T \frac{\partial \psi_1}{\partial x_1}\frac{\partial u_1}{\partial x_1} dt, \tag{A-4}$$

where

$$f \equiv \sqrt{\frac{V_{\text{nmo}}^2 - V_{S0}^2}{V_{P0}^2 - V_{S0}^2}}. \tag{A-5}$$

The second parameterization is defined as follows:

$$m_1 = \frac{V_{\text{nmo}}^2}{V_{\text{nmo},i}^2}, \tag{A-6}$$

$$m_2 = \frac{V_{S0}^2}{V_{S0,i}^2}, \tag{A-7}$$

$$m_3 = 1 + 2\eta, \tag{A-8}$$

$$m_4 = 1 + 2\delta, \tag{A-9}$$

where the subscript i in equations A-6 and A-7 denotes the initial parameters. The gradients for parameterization II are

$$\frac{\partial \mathcal{F}}{\partial m_1} = -\rho V_{\mathrm{nmo},i}^2 \int_0^T \left[(1+2\eta) \frac{\partial \psi_1}{\partial x_1} \frac{\partial u_1}{\partial x_1} + \frac{1}{1+2\delta} \frac{\partial \psi_3}{\partial x_3} \frac{\partial u_3}{\partial x_3} + \frac{1}{2} \left(\frac{f}{1+2\delta} + \frac{1}{2f} \right) \left(\frac{\partial \psi_3}{\partial x_3} \frac{\partial u_1}{\partial x_1} + \frac{\partial \psi_1}{\partial x_1} \frac{\partial u_3}{\partial x_3} \right) \right] dt, \tag{A-10}$$

$$\frac{\partial \mathcal{F}}{\partial m_2} = -\rho V_{S0,i}^2 \int_0^T \left[\left(\frac{\partial \psi_1}{\partial x_3} + \frac{\partial \psi_3}{\partial x_1} \right) \left(\frac{\partial u_1}{\partial x_3} + \frac{\partial u_3}{\partial x_1} \right) - \left(\frac{f}{2} + \frac{1}{2f} + 1 \right) \left(\frac{\partial \psi_3}{\partial x_3} \frac{\partial u_1}{\partial x_1} + \frac{\partial \psi_1}{\partial x_1} \frac{\partial u_3}{\partial x_3} \right) \right] dt, \tag{A-11}$$

$$\frac{\partial \mathcal{F}}{\partial m_3} = -\rho V_{\mathrm{nmo}}^2 \int_0^T \frac{\partial \psi_1}{\partial x_1} \frac{\partial u_1}{\partial x_1} dt, \tag{A-12}$$

$$\frac{\partial \mathcal{F}}{\partial m_4} = \frac{\rho V_{\mathrm{nmo}}^2}{(1+2\delta)^2} \int_0^T \left[\frac{\partial \psi_3}{\partial x_3} \frac{\partial u_3}{\partial x_3} + \frac{f}{2} \left(\frac{\partial \psi_3}{\partial x_3} \frac{\partial u_1}{\partial x_1} + \frac{\partial \psi_1}{\partial x_1} \frac{\partial u_3}{\partial x_3} \right) \right] dt. \tag{A-13}$$

For parameterization III,

$$m_1 = \frac{V_{\mathrm{hor}}^2}{V_{\mathrm{hor},i}^2}, \tag{A-14}$$

$$m_2 = \frac{V_{S0}^2}{V_{S0,i}^2}, \tag{A-15}$$

$$m_3 = 1 + 2\eta, \tag{A-16}$$

$$m_4 = 1 + 2\epsilon. \tag{A-17}$$

The gradients of the objective function are

$$\frac{\partial \mathcal{F}}{\partial m_1} = -\rho V_{\mathrm{hor},i}^2 \int_0^T \left[\frac{\partial \psi_1}{\partial x_1} \frac{\partial u_1}{\partial x_1} + \frac{1}{1+2\epsilon} \frac{\partial \psi_3}{\partial x_3} \frac{\partial u_3}{\partial x_3} + \frac{1}{2} \left(\frac{f}{1+2\epsilon} + \frac{1}{f(1+2\eta)} \right) \left(\frac{\partial \psi_3}{\partial x_3} \frac{\partial u_1}{\partial x_1} + \frac{\partial \psi_1}{\partial x_1} \frac{\partial u_3}{\partial x_3} \right) \right] dt, \tag{A-18}$$

$$\frac{\partial \mathcal{F}}{\partial m_2} = -\rho V_{S0,i}^2 \int_0^T \left[\left(\frac{\partial \psi_1}{\partial x_3} + \frac{\partial \psi_3}{\partial x_1} \right) \left(\frac{\partial u_1}{\partial x_3} + \frac{\partial u_3}{\partial x_1} \right) - \left(\frac{f}{2} + \frac{1}{2f} + 1 \right) \left(\frac{\partial \psi_3}{\partial x_3} \frac{\partial u_1}{\partial x_1} + \frac{\partial \psi_1}{\partial x_1} \frac{\partial u_3}{\partial x_3} \right) \right] dt, \tag{A-19}$$

$$\frac{\partial \mathcal{F}}{\partial m_3} = \frac{\rho V_{\mathrm{hor}}^2}{2f(1+2\eta)^2} \int_0^T \left(\frac{\partial \psi_3}{\partial x_3} \frac{\partial u_1}{\partial x_1} + \frac{\partial \psi_1}{\partial x_1} \frac{\partial u_3}{\partial x_3} \right) dt, \tag{A-20}$$

$$\frac{\partial \mathcal{F}}{\partial m_4} = \frac{\rho V_{\mathrm{hor}}^2}{(1+2\epsilon)^2} \int_0^T \left[\frac{\partial \psi_3}{\partial x_3} \frac{\partial u_3}{\partial x_3} + \frac{f}{2} \left(\frac{\partial \psi_3}{\partial x_3} \frac{\partial u_1}{\partial x_1} + \frac{\partial \psi_1}{\partial x_1} \frac{\partial u_3}{\partial x_3} \right) \right] dt. \tag{A-21}$$

If normalized density ($m_5 = \rho/\rho_i$) is included as a model parameter, the corresponding derivative of the objective function for parameterization III is

$$\frac{\partial \mathcal{F}}{\partial m_5} = -\rho_i \int_0^T \left\{ V_{\mathrm{hor}}^2 \frac{\partial \psi_1}{\partial x_1} \frac{\partial u_1}{\partial x_1} + V_{S0}^2 \left(\frac{\partial \psi_1}{\partial x_3} + \frac{\partial \psi_3}{\partial x_1} \right) \times \left(\frac{\partial u_1}{\partial x_3} + \frac{\partial u_3}{\partial x_1} \right) + \frac{V_{\mathrm{hor}}^2}{1+2\epsilon} \frac{\partial \psi_3}{\partial x_3} \frac{\partial u_3}{\partial x_3} + \left[\sqrt{\left(\frac{V_{\mathrm{hor}}^2}{1+2\epsilon} - V_{S0}^2 \right) \left(\frac{V_{\mathrm{hor}}^2}{1+2\eta} - V_{S0}^2 \right)} - V_{S0}^2 \right] \times \left(\frac{\partial \psi_3}{\partial x_3} \frac{\partial u_1}{\partial x_1} + \frac{\partial \psi_1}{\partial x_1} \frac{\partial u_3}{\partial x_3} \right) + \psi_1 \frac{\partial^2 u_1}{\partial t^2} + \psi_3 \frac{\partial^2 u_3}{\partial t^2} \right\} dt. \tag{A-22}$$

APPENDIX B

RADIATION PATTERNS FOR DIFFERENT PARAMETERIZATIONS

Kamath and Tsvankin (2016) derive radiation patterns for the stiffness coefficients of an anisotropic inclusion (scatterer) embedded in a homogeneous anisotropic background and compute expressions for model parameters in a transmission setup. To compute the radiation patterns for the model parameterizations considered here, the background is assumed to be isotropic, and the scatterers are considered to lie on a horizontal plane. The P-wave radiation patterns (normalized by $2\rho V_P$, where V_P is the background P-wave velocity) for parameterization I are as follows:

$$\Omega^P(V_{P0}) = \cos^2(\theta/2), \tag{B-1}$$

$$\Omega^P(V_{S0}) = 2g\sin^2\theta, \tag{B-2}$$

$$\Omega^P(V_{\mathrm{nmo}}) = \frac{1}{4}\sin^2\theta, \tag{B-3}$$

$$\Omega^P(V_{\mathrm{hor}}) = \sin^4(\theta/2), \tag{B-4}$$

where θ is the opening angle and $g = V_S/V_P$ (V_S is the S-wave velocity in the isotropic background). The patterns for the scattered SV-waves (normalized by $2\rho V_S$) are

$$\Omega^S(V_{P0}) = 0, \tag{B-5}$$

$$\Omega^S(V_{S0}) = \cos\,2\theta, \tag{B-6}$$

$$\Omega^S(V_{\mathrm{nmo}}) = \frac{1}{4g}\sin^2\theta, \tag{B-7}$$

$$\Omega^S(V_{\mathrm{hor}}) = \frac{1}{4g}\sin^2\theta. \tag{B-8}$$

For parameterization II, because the background is taken to be isotropic, the background values of V_{nmo} and V_P are equal. The P-wave radiation patterns (normalized by ρV_P^2) for this parameterization are

$$\Omega^P(V_{\mathrm{nmo}^2}) = 1, \tag{B-9}$$

$$\Omega^P(V_{S0}^2) = 2g^2\sin^2\theta, \tag{B-10}$$

$$\Omega^P(1+2\eta) = \sin^4(\theta/2), \tag{B-11}$$

$$\Omega^P(1+2\delta) = \cos^2(\theta/2). \tag{B-12}$$

The patterns for the scattered SV-wave (normalized by ρV_S^2) are

$$\Omega^S(V_{\mathrm{nmo}}^2) = 0, \tag{B-13}$$

$$\Omega^S(V_{S0}^2) = \cos\,2\theta, \tag{B-14}$$

$$\Omega^S(1+2\eta) = \frac{1}{4g^2}\sin^2\theta, \tag{B-15}$$

$$\Omega^S(1+2\delta) = 0. \tag{B-16}$$

For parameterization III, the background velocities V_{hor} and V_{P0} coincide. The P-wave radiation patterns then take the form:

$$\Omega^P(V_{\mathrm{hor}}^2) = 1, \tag{B-17}$$

$$\Omega^P(V_{S0}^2) = 2g^2\sin^2\theta, \tag{B-18}$$

$$\Omega^P(1+2\eta) = \frac{1}{4}\sin^2\theta, \tag{B-19}$$

$$\Omega^P(1+2\epsilon) = \cos^2(\theta/2). \tag{B-20}$$

The patterns for the scattered SV-wave (normalized by ρV_S^2) are

$$\Omega^S(V_{\mathrm{hor}}^2) = 0, \tag{B-21}$$

$$\Omega^S(V_{S0}^2) = \cos\,2\theta, \tag{B-22}$$

$$\Omega^S(1+2\eta) = \frac{1}{4g^2}\sin^2\theta, \tag{B-23}$$

$$\Omega^S(1+2\epsilon) = 0. \tag{B-24}$$

The P- and SV-wave radiation patterns for the normalized density (ρ/ρ_i) are

$$\Omega^P(\rho) = 2\cos^4(\theta/2), \tag{B-25}$$

$$\Omega^S(\rho) = 2\,\cos(3\theta/2)\cos(\theta/2). \tag{B-26}$$

REFERENCES

Alkhalifah, T., 2015, Research note: Insights into the data dependency on anisotropy: An inversion prospective: Geophysical Prospecting, **64**, 505–513, doi: 10.1111/1365-2478.12345.

Alkhalifah, T., and R. Plessix, 2014, A recipe for practical full-waveform inversion in anisotropic media: An analytical parameter resolution study: Geophysics, **79**, no. 3, R91–R101, doi: 10.1190/geo2013-0366.1.

Bunks, C., F. M. Saleck, S. Zaleski, and G. Chavent, 1995, Multiscale seismic waveform inversion: Geophysics, **60**, 1457–1473, doi: 10.1190/1.1443880.

Byrd, R. H., P. Lu, J. Nocedal, and C. Zhu, 1995, A limited memory algorithm for bound constrained optimization: SIAM Journal on Scientific Computing, **16**, 1190–1208, doi: 10.1137/0916069.

Duan, Y., P. Sava, and A. Guitton, 2017, Elastic least-squares reverse time migration: Geophysics, **82**, no. 4, S315–S325, doi: 10.1190/geo2016-0564.1.

Gardner, G. H. F., L. W. Gardner, and A. R. Gregory, 1974, Formation velocity and density — The diagnostic basics for stratigraphic traps: Geophysics, **39**, 770–780, doi: 10.1190/1.1440465.

Gholami, Y., R. Brossier, S. Operto, A. Ribodetti, and J. Virieux, 2013a, Which parameterization is suitable for acoustic vertical transverse isotropic full waveform inversion? Part 2 — Synthetic and real data case studies from Valhall: Geophysics, **78**, no. 2, R107–R124, doi: 10.1190/GEO2012-0203.1.

Gholami, Y., R. Brossier, S. Operto, A. Ribodetti, and J. Virieux, 2013b, Which parameterization is suitable for acoustic vertical transverse isotropic full waveform inversion? Part 1 — Sensitivity and trade-off analysis: Geophysics, **78**, no. 2, R81–R105, doi: 10.1190/geo2012-0204.1.

Kamath, N., and I. Tsvankin, 2013, Full-waveform inversion of multicomponent data for horizontally layered VTI media: Geophysics, **78**, no. 5, WC113–WC121, doi: 10.1190/geo2012-0415.1.

Kamath, N., and I. Tsvankin, 2016, Elastic full-waveform inversion for VTI media: Methodology and sensitivity analysis: Geophysics, **81**, no. 2, C53–C68, doi: 10.1190/geo2014-0586.1.

Lee, H., J. M. Koo, D. Min, B. Kwon, and H. S. Yoo, 2010, Frequency-domain elastic full waveform inversion for VTI media: Geophysical Journal International, **183**, 884–904, doi: 10.1111/j.1365-246X.2010.04767.x.

Munns, J., 1985, The Valhall field: A geological overview: Marine and Petroleum Geology, **2**, 23–43, doi: 10.1016/0264-8172(85)90046-7.

Oh, J.-W., and T. Alkhalifah, 2016, Elastic orthorhombic anisotropic parameter inversion: An analysis of parameterization: Geophysics, **81**, no. 6, C279–C293, doi: 10.1190/geo2015-0656.1.

Operto, S., Y. Gholami, T. Alkhalifah, V. Prieux, A. Ribodetti, R. Brossier, L. Metivier, and J. Virieux, 2013, A guided tour of multiparameter full-waveform inversion with multicomponent data: From theory to practice: The Leading Edge, **32**, 1040–1054, doi: 10.1190/tle32091040.1.

Plessix, R., and Q. Cao, 2011, A parameterization study for surface seismic full waveform inversion in an acoustic vertical transversely isotropic medium: Geophysical Journal International, **185**, 539–556, doi: 10.1111/j.1365-246X.2011.04957.x.

Prieux, V., R. Brossier, S. Operto, and J. Virieux, 2013, Multiparameter full waveform inversion of multicomponent ocean-bottom-cable data from the Valhall field. Part 2 — Imaging compressive-wave and shear-wave velocities: Geophysical Journal International, **194**, 1665–1681, doi: 10.1093/gji/ggt178.

Sears, T. J., P. J. Barton, and S. C. Singh, 2010, Elastic full waveform inversion of multicomponent ocean-bottom cable seismic data: Application to Alba Field, U.K. North Sea: Geophysics, **75**, no. 6, R109–R119, doi: 10.1190/1.3484097.

Sears, T. J., S. C. Singh, and P. J. Barton, 2008, Elastic full waveform inversion of multicomponent OBC seismic data: Geophysical Prospecting, **56**, 843–862, doi: 10.1093/gji/ggt178.

Tarantola, A., 1984, Linearized inversion of seismic reflection data: Geophysical Prospecting, **32**, 998–1015, doi: 10.1111/j.1365-2478.1984.tb00751.x.

Tsvankin, I., 2012, Seismic signatures and analysis of reflection data in anisotropic media, 3rd ed.: SEG.

Vigh, D., K. Jiao, D. Watts, and D. Sun, 2014, Elastic full-waveform inversion application using multicomponent measurements of seismic data collection: Geophysics, **79**, no. 2, R63–R77, doi: 10.1190/geo2013-0055.1.

Williamson, P. R., 1991, A guide to the limits of resolution imposed by scattering in ray tomography: Geophysics, **56**, 202–207, doi: 10.1190/1.1443032.

Wu, R., and M. Toksöz, 1987, Diffraction tomography and multisource holography applied to seismic imaging: Geophysics, **52**, 11–25, doi: 10.1190/1.1442237.